Supporting Information

Ion-Pair and Solvation Engineering for High-Potential Organic Catholytes in Aqueous Flow Batteries

Wenxuan Fu, Puiki Leung*, Shuai Liu, Yong Zuo, Tadele H. Wondimu, Akeel A. Shah, Frank C. Walsh, Qian Xu*, Qiang Liao

Table S1. Benchmarking comparison of representative AORFB catholytes in terms of redox potential, solubility, decay rate, theoretical energy density, and estimated material cost. Note: Estimated material costs are approximate laboratory-scale prices obtained from commercial suppliers or structurally similar prototype compounds. System-level costs ($ kWh^{-1}) depend strongly on full-cell configuration and operating conditions and are therefore not directly compared here.

Catholyte	Redox Potential (V vs. SHE)	Solubility (M)	Decay Rate (%/cycle)	Theoretical Energy Density (Wh L^{-1}, catholyte only)	Estimated material cost ($ kg^{-1})	Notes / Ref
4-NPEA·HBr (this work)	**1.24**	**>0.7**	**<0.085**	**~62 (0.7 M, 4e⁻)**	**~143**	**Br^- SSIP for transport, 4e⁻ PCET**
QCA (quinoxaline anolyte, paired to $K_4Fe(CN)_6$)	-0.79	5.5	0.1	-	~3400	High solubility anolyte for 1.28 V cell [1]
Viologen (halide)	0.8–1.0	1.0	0.05	40–50 (2e⁻)	~6×10^4	Halide reduces dimerization [2]
Phenazine (halide)	0.9–1.05	0.6–0.9	~0.2	30–40 (2e⁻)	~500 – 2000	Halide improves solubility [3]
Tri-TEMPO (non-aq.)	0.57	0.5	0.19	~24 (0.5 M, 3e⁻)	~3×10^4	Multi-electron TEMPO catholyte for non-aqueous RFB [4]
1,6-DPAP (phenazine anolyte)	-0.08	1.0	-	~4 (1 M, 2e⁻)	~500 – 2000	Low cost anolyte [5]
Ferrocene (FcN_2Br_2)	0.61	1.0	0.2	~16 (1e⁻)	~500 – 2000	Halide for solubility [6]
$Na_4[FeII(Dcbpy)_2(CN)_2$	0.85	1.0	<0.1	~23	~1000 – 5000	Fe-bipyridine coordination catholyte [7]
Vanadium (inorganic catholyte)	1.0	1.6	<0.1	20–35	~100	Benchmark inorganic catholyte [8]

Note: Estimated material costs are based on commercially available laboratory-scale reagent prices or representative precursor costs reported in the literature, rather than bulk industrial production costs. In particular, the ~143 $ kg^{-1} value for 4-NPEA·HBr is derived from laboratory-scale commercial pricing and does not represent large-scale industrial production cost. These values are provided for qualitative comparison of relative economic feasibility.

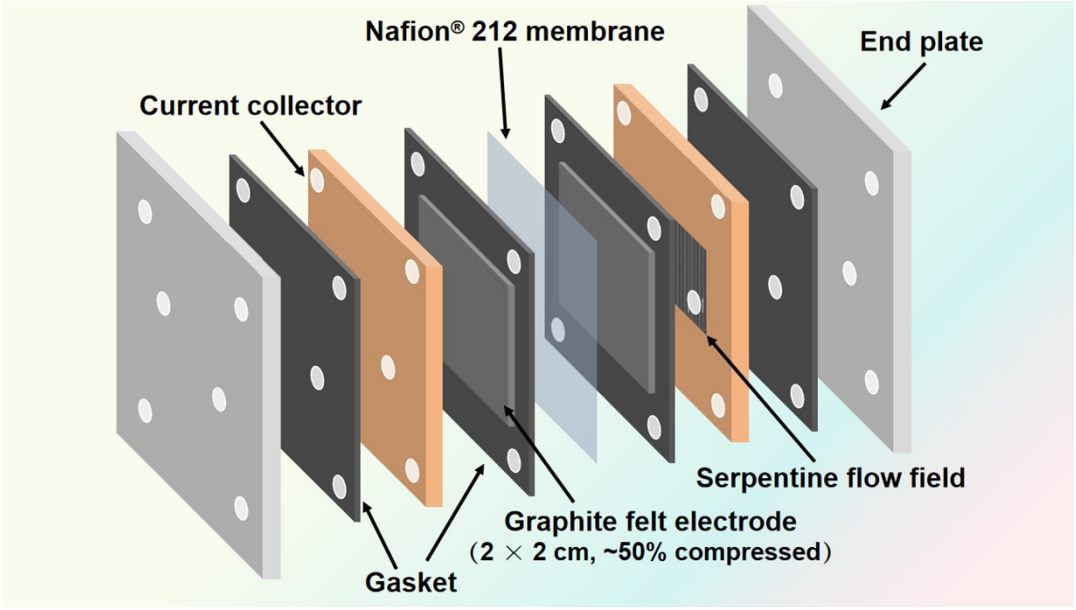

Figure S1. Exploded schematic of the single-cell flow battery assembly used in this study. The components include end plates, current collector with serpentine flow field, PTFE gasket (1 mm thick), heat-treated graphite felt electrode (2 × 2 cm, ~50% compressed), Nafion® 212 membrane. The active geometric area is 4 cm^2 and electrolytes are circulated at 50 mL min^{-1}.

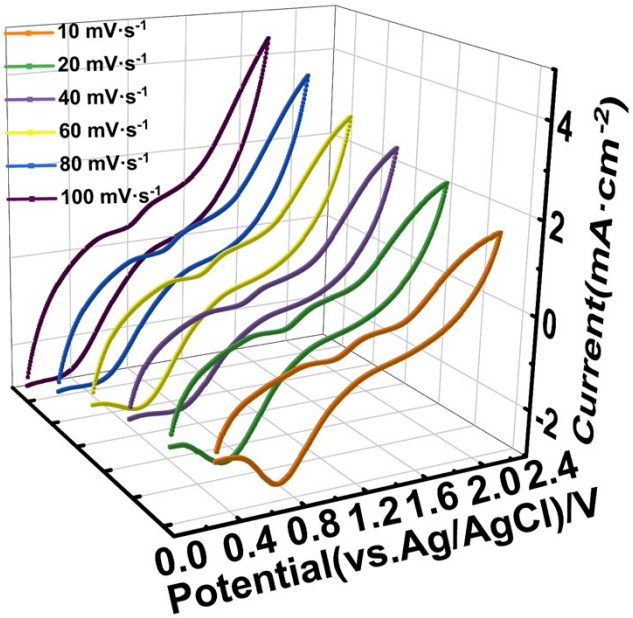

Figure S2. CV curves of 0.1 M 4-NPEA·HBr in 1 M HCl at different scan rates (10–100 mV s^{-1}) on thermally treated graphite felt electrode.

Table S2. Key parameters used in the numerical simulation model.

Symbols	Parameters	Value	Unit
N_{mesh}	Number of elements	55895	–
c_{pos}^{0}	Initial concentration of $4-NPEA{\cdot}HBr$	100	$mol{\cdot}m^{-3}$
c_{Cl}^{0}	Initial concentration of Cl^-	1000	$mol{\cdot}m^{-3}$
D_{pos}	Diffusion coefficient of $4-NPEA{\cdot}HBr$	1.32×10^{-9}	$m^2{\cdot}s^{-1}$
E_{pos}^{0}	Equilibrium potential: positive	1.035	V
$\sigma_{s}GF$	GF conductivity	220	$S{\cdot}m^{-1}$
σ_{m}	Membrane conductivity	0.3	$S{\cdot}m^{-1}$
σ_{pos}	Conductivity of positive electrolyte	38	$S{\cdot}m^{-1}$
T	Temperature	298.15	K
i_{app}	Applied current density	–	$A{\cdot}m^{-2}$
$d_{f}GF$	Carbon fiber diameter	1.5×10^{-5}	m
$k_{pos}GF$	Reaction rate constant of positive	6.25×10^{-5}	$m{\cdot}s^{-1}$
$\alpha_{1}GF$	transfer coefficient of positive	0.424	–
K_{CK}	Carman–Kozeny constant	5.55	–
ε_{GF}	Electrode porosity	0.95	–
a_{GF}	Specific surface area of GF	673272	m^{-1}
F	Faraday constant	96485	$C{\cdot}mol^{-1}$
Q	Volumetric flow rate	50	$mL{\cdot}min^{-1}$
W_e	Width of electrode	0.02	m

H_e	Height of electrode	0.02	m
L_GF	Electrode thickness	0.002	m
L_M	Membrane thickness	7×10^{-4}	m

Table S3. i_{pc}/i_{pa} ratios at different scan rates.

Scan rate (mV s^{-1})	i_{pa} (mA cm^{-2})	i_{pc} (mA cm^{-2})	i_{pc}/i_{pa}
10	128	-83	0.65
20	295	-305	1.03
40	391	-443	1.13
60	461	-530	1.14
80	532	-559	1.05
100	600	-591	0.99

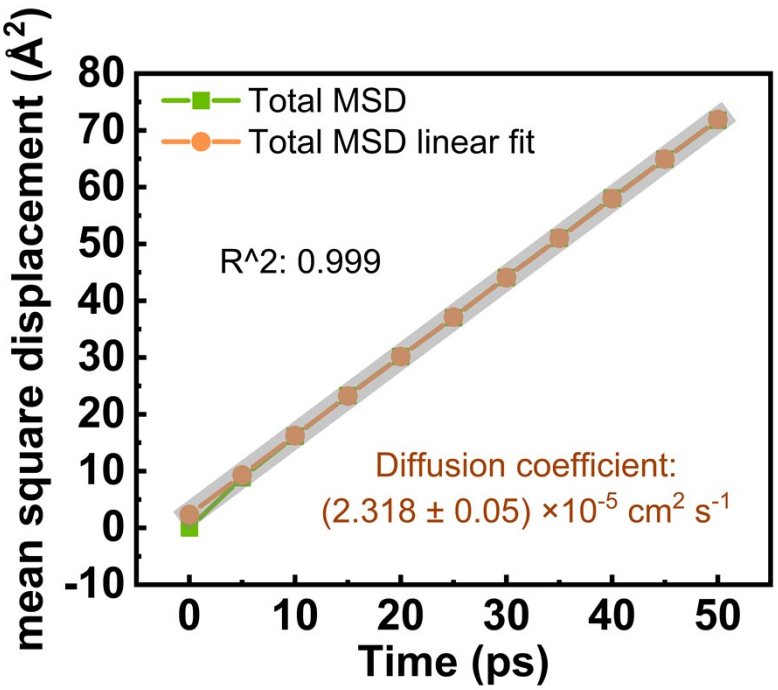

Figure S3. The mean square displacement curve of 4-NPEA·HBr, The shaded region represents the statistical uncertainty obtained from trajectory sampling.

Table S4. Comparison of diffusion coefficients from CV (using different assumed n) and MD simulation.

Assumed n	D from CV ($cm^2 s^{-1}$)	Deviation factor from MD ($2.32 \times 10^{-5} cm^2 s^{-1}$)	Consistency
1	~8.45×10^{-4}	~ 36 × higher (unrealistic)	Poor
2	~1.06×10^{-4}	~ 4.6 × higher	Inconsistent
4	**1.32×10^{-5}**	**~ 1.76 × lower**	**Excellent**
6	~3.9×10^{-6}	~ 6 × lower	Unrealistic

Table S5. Summary of density functional theory calculation data.

Compound	DFT Optimization Parameters			Solvation Free Energy (PCM, Water)	
	E(OPT) (a.u.)	Conv. Criteria	-V/T	ΔG(solv) (kcal/mol)	E(PCM) (a.u.)
4-NPEA·HBr	-3142.911	0.19D-08	2.0067	-21.42	-3143.148
4-HPEA·HBr	-3069.108	0.94D-08	2.0068	-24.88	-3069.169

S3.2.1. Density Functional Theory (DFT) Analysis of Electronic Structure

For the oxidized state, exhibits a LUMO energy level of –2.91 eV, which is more negative than those of common organic positive materials (e.g. quinones, LUMO ≈ –1.5 to –2.0 eV), indicating stronger electron affinity and suggesting a higher reduction potential. The LUMO electron density is highly localized on the nitro group (-NO_2)

and the attached benzene ring, confirming the nitro group as the primary reduction active center. The conjugated benzene ring facilitates electron delocalization, further enhancing reaction kinetics. The HOMO level (–6.34 eV) lies above the OER threshold, ensuring antioxidative stability. This stability suppresses the OER, which is essential for achieving high-potential aqueous batteries. The HOMO-LUMO gap (ΔE) of 3.43 eV indicates the molecular stability and feasibility of redox reactions, consistent with the reversible electrochemical behavior observed.

In the reduced state, 4-HPEA·HBr shows a higher HOMO energy level (–5.93 eV), suggesting that the hydroxylamine group is more readily oxidized back to the nitro group during charging. The HOMO electron density is primarily localized on the lone pair electrons of the hydroxylamine group, confirming it as the electron-donating center (oxidation active site), consistent with the high reversibility observed in electrochemical tests. Furthermore, the HOMO density extends partially to the Br^- ion and the benzene ring, indicating that Br^- stabilizes the reduced structure through coordination. The HOMO density partially delocalized onto Br^- suggests through-space electronic coupling, potentially aided by the conjugated ring. The relatively high LUMO energy level (–1.00 eV) indicates weaker electron affinity, which helps prevent irreversible side reactions caused by over-reduction, thereby enhancing cycling stability. And the larger ΔE (4.88 eV) indicates higher kinetic stability in the reduced state.

Solvation free energy calculations reveal $\Delta G_{(solv)}$ values of –21.42 kcal/mol for 4-NPEA·HBr and –24.88 kcal/mol for 4-HPEA·HBr , confirming the thermodynamic stability of both states and supporting the stabilization of the reduced state by Br^- coordination ($\Delta\Delta G_{(solv)}$ = –3.46 kcal/mol). The elevated HOMO level of 4-HPEA·HBr, along with the stabilizing effect of the Br^- ion interaction, reinforces the thermodynamic spontaneity of the hydroxylamine oxidation to nitro, contributing to the observed cycling stability and slow capacity decay.

When comparing the impact of different anions, 4-NPEA·HBr and 4-NPEA·HCl exhibit similar LUMO energy levels and nearly identical electron density distribution patterns. However, the HOMO energy level of 4-NPEA·HCl is markedly lower (–7.78

eV), with electron density extensively delocalized over the Cl^- ion, the benzene ring, and the amine group. This extensive hybridization results from the small radius, high electronegativity and low polarizability of Cl^-, favoring strong electrostatic ionic bonding interactions with the organic cation.

S3.2.2. MD Simulations of Diffusion and Solvation

RDF analysis (**Figure 3d** and **Table S6**) revealed fundamental differences in the interactions of Br^- and Cl^- with the nitro group oxygen atoms (O_nitro). For 4-NPEA·HBr (Br^--O_nitro), the first RDF peak position at *ca*. 5.45 Å indicates a solvent-separated ion pair (SSIP) configuration, mediated by water molecule bridging. The corresponding *g*(r) peak value of ≈ 7.0 indicates a high probability of finding the Br^- ion at this specific distance from O_nitro, reflecting a strong spatial correlation between them in the solution. In contrast, for 4-NPEA·HCl (Cl^--O_nitro), the first RDF peak at *ca*. 3.65 Å (*g*(r) ≈ 1.2) is characteristic of a contact ion pair (CIP) configuration, where direct electrostatic interaction occurs. The coordination number (CN), obtained by integrating the RDF up to 7.0 Å, provides complementary insight into the local association behavior. The CN value for Cl^--O_nitro (CN@7.0 Å ≈ 0.13) is higher than that for Br^--O_nitro (CN@7.0 Å ≈ 0.053), indicating a higher probability of direct and frequent ion-dipole contact in the Cl^- system, consistent with the formation of a CIP. In contrast, the lower CN observed for Br^- does not imply weaker interaction, but rather reflects the SSIP configuration, where Br^- is predominantly separated from O_nitro by one or more intervening water molecules. In this case, the interaction is characterized by a well-defined spatial correlation, as evidenced by the pronounced RDF peak at ~5.45 Å with a high g(r) value (~7.0), while the reduced CN reflects the transient and indirect nature of Br^- coordination. Although quantitative prediction of viscosity and conductivity is beyond the primary scope of this MD study, The solvent-separated ion-pair configuration observed in the Br^- system is expected to reduce ion clustering and facilitate molecular mobility, consistent with literature models for ion-paired organic electrolytes.[9]

Table S6. Summary table of Radial distribution Function Results.

Parameters	Br-O_{nitro}	Cl-O_{nitro}	Multiple of difference
The position of the first peak	5.45 ± 0.05 Å	3.65 ± 0.05 Å	~1.49 times
The height of the first peak	7.0 ± 0.2	1.2 ± 0.1	~5.83 times
Coordination number	0.053 ± 0.005	0.13 ± 0.01	~0.41 times
Interaction type	Solvent separation of ion pairs	Contact ion pair	—

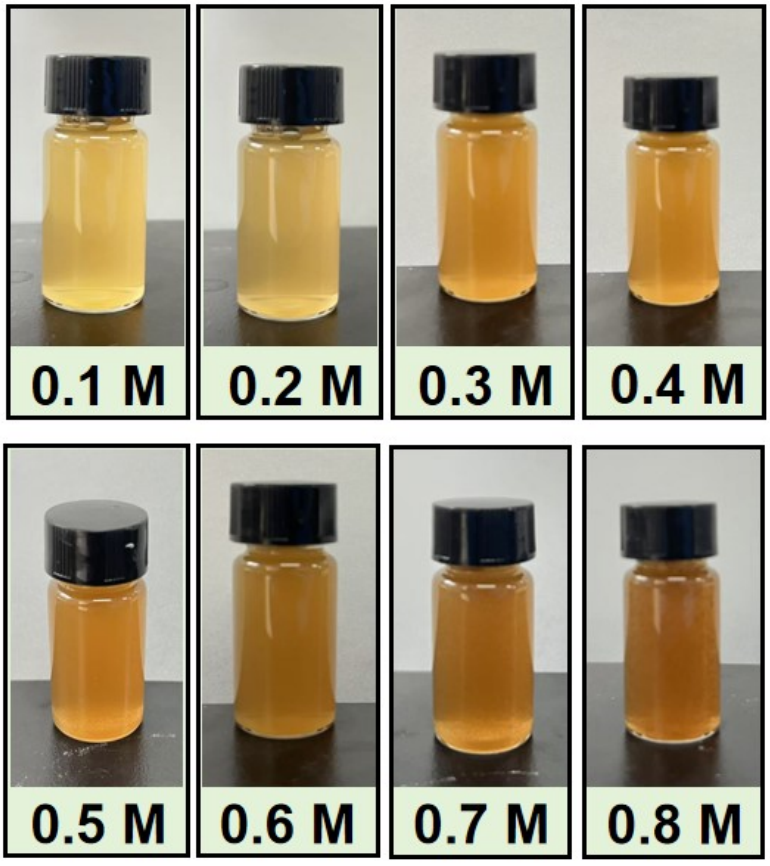

Figure S4. Test of the solubility of 4-NPEA • HBr in 1 M HCl.

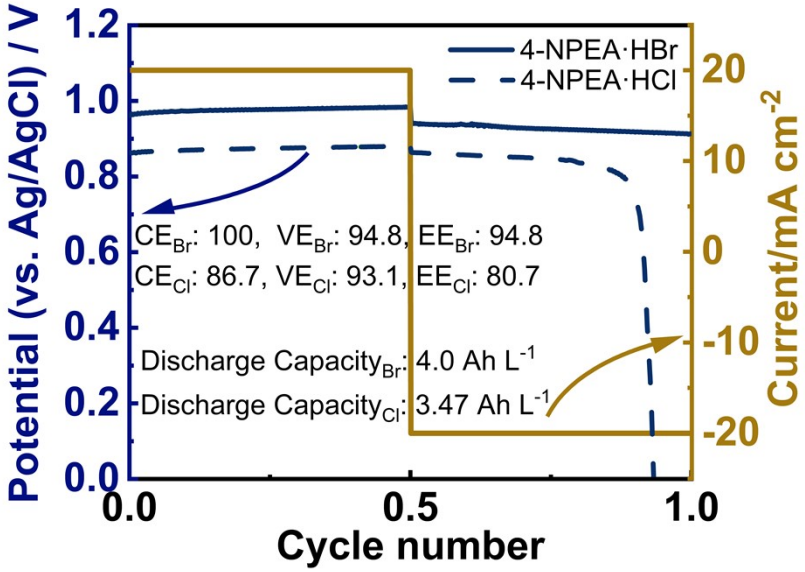

Figure S5. Charge-discharge profiles of 4-NPEA·HBr and 4-NPEA·HCl.

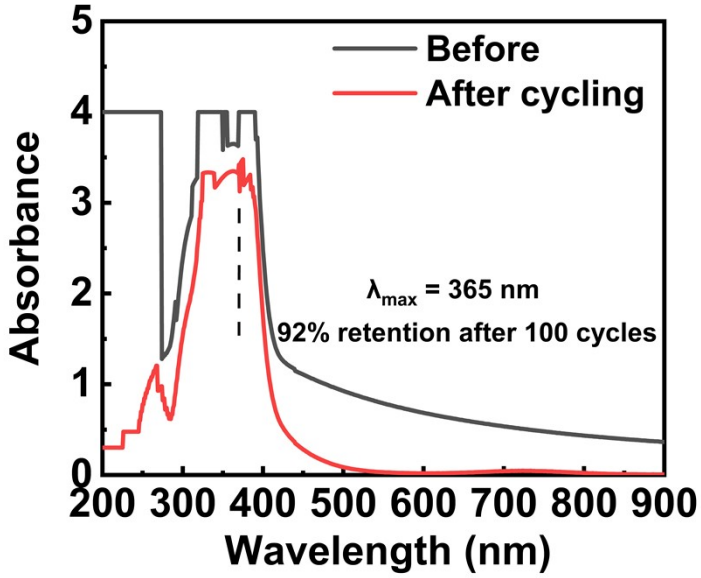

Figure S6. UV-*vis* spectra of the catholyte before and after cycling.

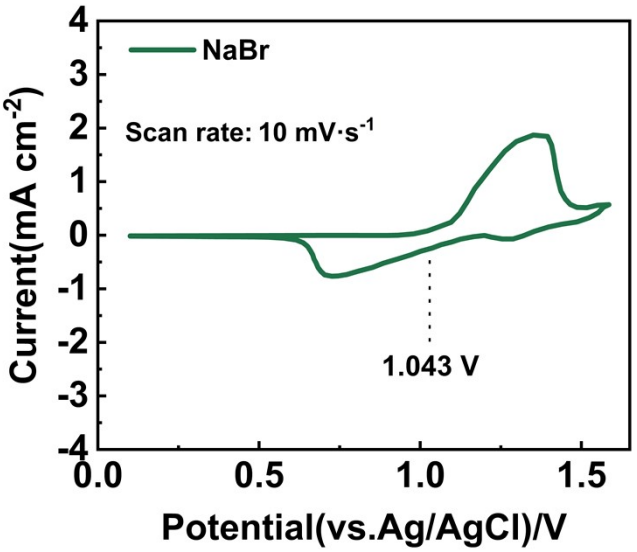

Figure S7. Cyclic voltammogram of 0.1 M NaBr in 1 M HCl (no 4-NPEA·HBr) on thermally treated graphite felt electrode (scan rate 10 mV s^{-1}). The anodic current density remains negligible (< 0.3 mA cm^{-2}) up to approximately 1.1 V vs. Ag/AgCl (corresponding to ~1.3 V vs. SHE), with the oxidation peak appearing at higher potentials. This demonstrates a substantial kinetic overpotential for Br^-/Br_2 oxidation, confirming bromide remains electrochemically inactive in the catholyte operating window (~1.24 V vs. SHE). Dashed line marks the equivalent operating potential (1.043 V vs. Ag/AgCl, corresponding to 1.24 V vs. SHE).

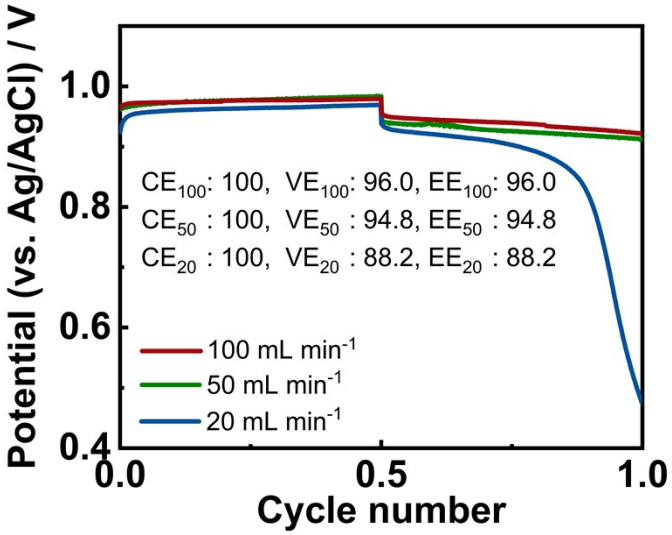

Figure S8. Charge–discharge voltage profiles of the 4-NPEA·HBr flow cell at different electrolyte flow rates (20, 50, and 100 mL min^{-1}).

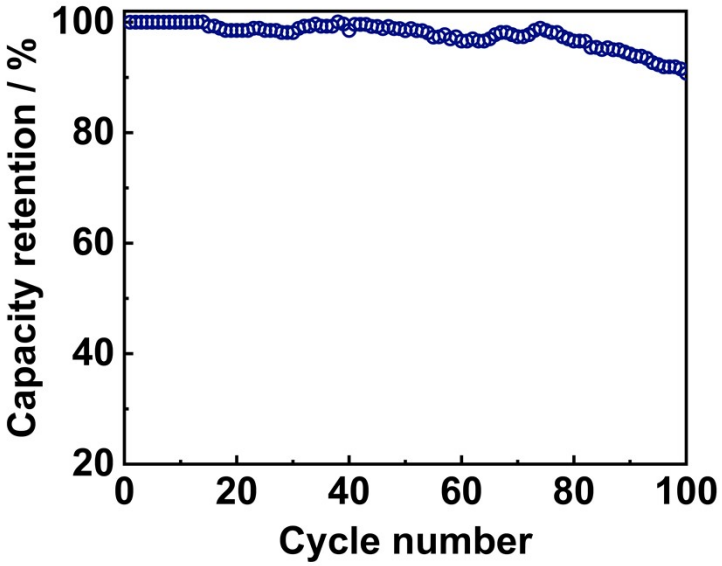

Figure S9. Capacity retention of the 4-NPEA·HBr electrolyte during 100 galvanostatic charge–discharge cycles.

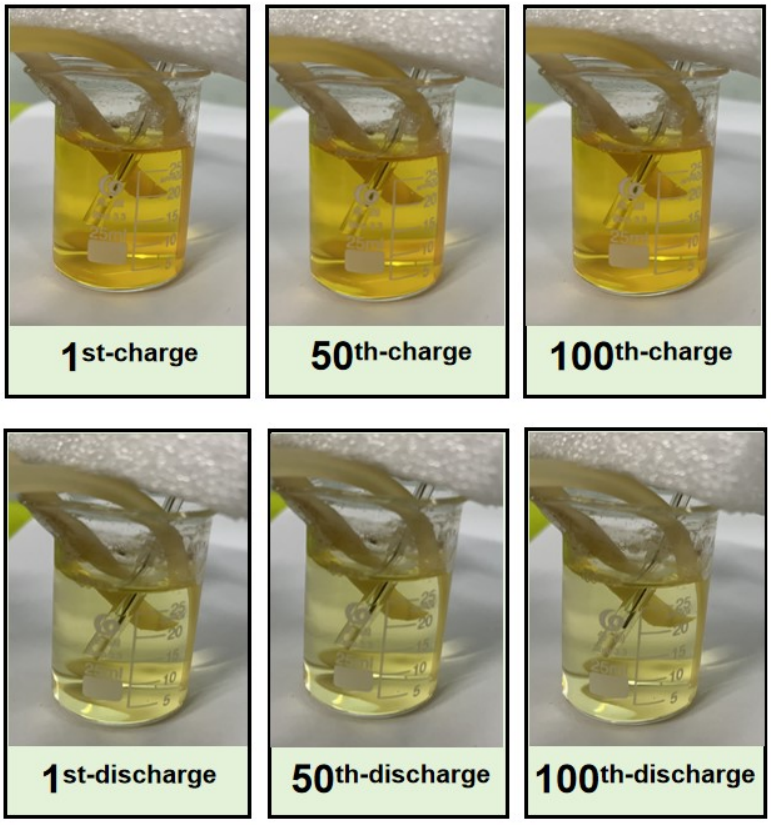

Figure S10. Reversible electrolyte color evolution with SOC during long-term cycling.

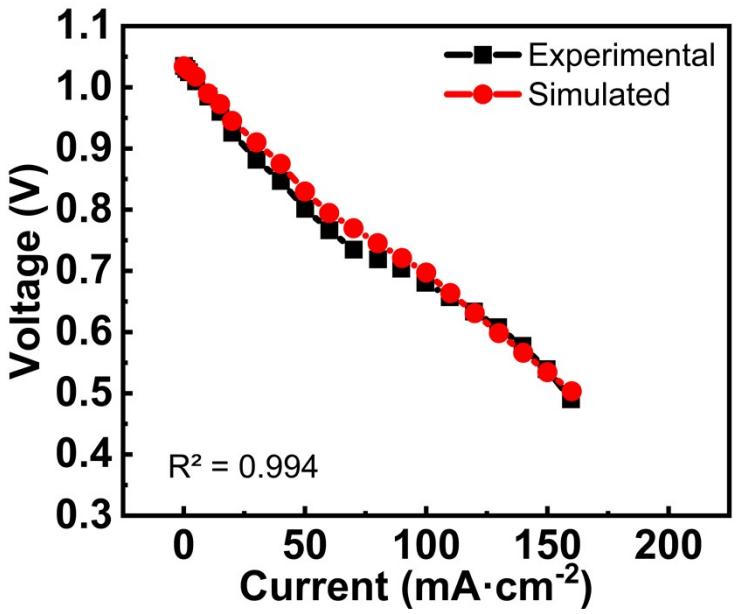

Figure S11. Comparison of simulated and experimental values of the 4-NPEA·HBr.

Table S7. Grid independence of voltage and pressure drop.

Number of grids	Pressure drop (Pa)	Output voltage (V)
40781	2621.9	1.0414
44196	2630.3	1.0412
48369	2631.0	1.0411
51051	2642.8	1.0410
53778	2660.7	1.0410
55895	2662.2	1.0410

Raw electrochemical data for the CV curves are provided in **Dataset S1**.

The raw UV–*vis* spectral data used to generate **Figure S6** are provided in **Dataset S2** in the Supporting Information.

References (Supporting Information)

1 C. Wang, Y. Wang, M. Tao, B. Yu, K. Zhang, J. Wei, Y. Liu, P. Zhang, G. Ding, Z. Tie, J. Cao, and Z. Jin, C. Wang, Y. Wang, M. Tao, B. Yu, K. Zhang, J. Wei, Y. Liu, P. Zhang, G. Ding, Z. Tie, J. Cao, and Z. Jin, *ACS Appl. Energy Mater.*, 2022, **5**, 10379-10384;

2 T. Yin, J. Duanmu, and L. Liu, T. Yin, J. Duanmu, and L. Liu, *J. Mater. Chem. A*, 2024, **12**, 15519-15540;

3 C. Ye, A. Wang, C. Breakwell, R. Tan, C. Grazia Bezzu, E. Hunter-Sellars, D. R. Williams, N. P. Brandon, P. A. A. Klusener, A. R. Kucernak, K. E. Jelfs, N. B. McKeown, and Q. Song, C. Ye, A. Wang, C. Breakwell, R. Tan, C. Grazia Bezzu, E. Hunter-Sellars, D. R. Williams, N. P. Brandon, P. A. A. Klusener, A. R. Kucernak, K. E. Jelfs, N. B. McKeown, and Q. Song, *Nat. Commun.*, 2022, **13**, 3184;

4 R. K. Gautam, X. Wang, A. Lashgari, S. Sinha, J. McGrath, and R. S. J. J. Jiang, R. K. Gautam, X. Wang, A. Lashgari, S. Sinha, J. McGrath, and R. S. J. J. Jiang, *Nat Commun*, 2023, **14**, 4753;

5 D. Emmel, S. Kunz, N. Blume, Y. Kwon, T. Turek, C. Minke, and D. Schroder, D. Emmel, S. Kunz, N. Blume, Y. Kwon, T. Turek, C. Minke, and D. Schroder, *Nat Commun*, 2023, **14**, 6672;

6 B. Hu, C. DeBruler, Z. Rhodes, and T. L. Liu, B. Hu, C. DeBruler, Z. Rhodes, and T. L. Liu, *J. Am. Chem. Soc.*, 2017, **139**, 1207-1214;

7 X. Li, P. Gao, Y.-Y. Lai, J. D. Bazak, A. Hollas, H.-Y. Lin, V. Murugesan, S. Zhang, C.-F. Cheng, W.-Y. Tung, Y.-T. Lai, R. Feng, J. Wang, C.-L. Wang, W. Wang, and Y. Zhu, X. Li, P. Gao, Y.-Y. Lai, J. D. Bazak, A. Hollas, H.-Y. Lin, V. Murugesan, S. Zhang, C.-F. Cheng, W.-Y. Tung, Y.-T. Lai, R. Feng, J. Wang, C.-L. Wang, W. Wang, and Y. Zhu, *Nat. Energy*, 2021, **6**, 873-881;

8 P. Leung, A. A. Shah, L. Sanz, C. Flox, J. R. Morante, Q. Xu, M. R. Mohamed, C. Ponce de León, and F. C. Walsh, P. Leung, A. A. Shah, L. Sanz, C. Flox, J. R. Morante, Q. Xu, M. R. Mohamed, C. Ponce de León, and F. C. Walsh, *J. Power Sources*, 2017, **360**, 243-283;

9 A. Falsafi and H. Nejat Pishkenari, A. Falsafi and H. Nejat Pishkenari, *The Journal of Physical Chemistry C*, 2016, **120**, 26259-26269;